

Lessons on early structure formation from a mature galaxy cluster observed at cosmic noon

Boyuan Liu[✉]¹, Anna T. P. Schauer[†]¹, and Volker Bromm¹

¹*Department of Astronomy, University of Texas, Austin, TX 78712, USA*

Accepted XXX. Received YYY; in original form ZZZ

ABSTRACT

We demonstrate a new approach of indirectly constraining both early star and structure formation via mature galaxy clusters at cosmic noon ($z \sim 2$), using the cluster XLSSC 122 as an example. With the standard Press Schechter formalism, we infer a rapid evolution of the star formation efficiency (the ratio of stellar to halo mass) from 10^{-4} to 0.01 during $z \sim 20 - 13$, based on the age distribution of stars in post-starburst galaxies of XLSSC 122, measured by HST photometry assuming no dust extinction. Here, we consider all low-mass haloes, including minihaloes, that host the first stars and galaxies ($5 \times 10^5 M_\odot \lesssim M_{\text{halo}} \lesssim 10^{10} M_\odot$). We also place new constraints on fuzzy dark matter models of $m_a \lesssim 5 \times 10^{-21} \text{ eV}/c^2$ for the ultra-light boson mass, from the abundance of galaxies with star formation at $z \gtrsim 13$ in XLSSC 122. Our exploratory results are consistent with existing constraints. More comprehensive results will be obtained if our approach is extended to a large sample of clusters or field post-starburst galaxies at cosmic noon, with improved modelling of halo and stellar populations.

Key words: early universe – dark ages, reionization, first stars – dark matter

1 INTRODUCTION

A grand challenge for modern astrophysics is to constrain star and galaxy formation in the first billion years of cosmic history (Loeb & Furlanetto 2013). This is in particular the case for the first, so-called Population III (Pop III), stars and galaxies formed at $z \gtrsim 10$, which are believed to have distinct features compared with their present-day counterparts (reviewed by e.g. Bromm & Yoshida 2011; Bromm 2013). Future facilities, such as the *James Webb Space Telescope* (*JWST*) and the Einstein Telescope (ET), are expected to directly probe this formative epoch (e.g. Appleton et al. 2009; Pawlik et al. 2011; Zackrisson et al. 2017; Jeon & Bromm 2019; Basu-Zych et al. 2019; Maggiori et al. 2020). However, before they come into operation, we have to rely on indirect observations and empirical constraints.

A traditional indirect approach is ‘stellar archaeology’, where clues to the earliest star-forming environments are derived from local ($z \sim 0$) observations of extremely metal poor (EMP) stars ($[\text{Fe}/\text{H}] < -3$; e.g. Frebel & Norris 2015; Ji et al. 2015). For instance, the non-detection of metal-free stars in the Milky Way place constraints on the low-mass end ($\lesssim 0.8 M_\odot$) of the Pop III initial mass function (IMF) (Hartwig et al. 2015; Maggiori et al. 2019), while

the abundance patterns of observed EMP stars constrain the higher-mass ($\gtrsim 10 M_\odot$) regime of the Pop III IMF, as well as the properties of the first supernovae (Ishigaki et al. 2018). Another probe that has become promising recently is the 21-cm signal from high- z neutral hydrogen, encoding the Lyman- α and X-ray fields powered by the first stars and galaxies (e.g. Mirocha & Furlanetto 2019; Fialkov & Barkana 2019; Qin et al. 2020). As a specific example, Schauer et al. (2019b) found that Pop III star formation in minihaloes ($M_{\text{halo}} \sim 10^6 M_\odot$) is required to explain the timing ($z \sim 17$) of the 21-cm absorption signal potentially detected by the Experiment to Detect the Global Epoch of Reionization Signature (EDGES; Bowman et al. 2018). Each approach is subject to uncertainties, such as turbulent metal mixing in the formation pathways of EMP stars, or the escape fraction of Lyman- α photons. It is therefore important to harness new probes to complement the existing ones.

In this work, we consider mature galaxy clusters at cosmic noon ($z \sim 2$) to constrain early star and structure formation, e.g. IDCS J1426.5+3508 ($z = 1.75$; Stanford et al. 2012), JKCS 041 ($z = 1.8$; Andreon et al. 2014; Newman et al. 2014), Cl J1449+0856 ($z = 2$; Gobat et al. 2013; Strazzullo et al. 2016), and XLSSC 122 ($z = 1.98$; Mantz et al. 2018; Willis et al. 2020). These clusters are the most massive virialized structures in the Universe $\sim 3 - 4$ Gyr after the Big Bang, such that their oldest constituent post-starburst galaxies (i.e. red-sequence cluster members) probe

* E-mail: boyuan@utexas.edu

† Hubble Fellow

star formation histories at much earlier times ($z \gtrsim 10$). Here, we consider XLSSC 122 to demonstrate our basic approach, given the cluster's clear post-starburst red-sequence members with ages of $t_w \sim 2.4 - 3.1$ Gyr. We construct an idealized stellar population model, based on the standard extended Press-Schechter (EPS) formalism (Sec. 2), to derive new constraints on early star formation parameters and dark matter (DM) physics from the age distribution of stars within the XLSSC 122 red sequence (Sec. 3), as measured by the Hubble Space Telescope (HST; Willis et al. 2020). We summarize our findings and discuss future directions in Section 4.

2 STELLAR POPULATION MODEL

The cluster XLSSC 122 is observed at $z_{\text{obs}} = 1.98$ (Willis et al. 2020). X-ray observations show that it has a virial mass of $M_2 \sim 10^{14} M_\odot$, a virial (physical) radius of $r_{200} \approx 1.5r_{500} \simeq 440$ kpc, and a sound-crossing time of $t_{\text{cr}} \simeq 3.3 \times 10^8$ yr (Mantz et al. 2018). To connect the observed luminosity-weighted posterior age distribution of (red-sequence) galaxies in XLSSC 122 to star and structure formation at higher redshifts ($z \gtrsim 13$) with a simple but flexible model, we employ the standard EPS formalism (Mo et al. 2010) to estimate halo abundances. We further make the following assumptions and approximations:

- XLSSC was formed at $z_2 \simeq 2.8$, i.e. 3 sound-crossing timescales before the observed epoch ($t_{\text{cr}} \simeq 3.3 \times 10^8$ yr)¹.
- Star formation in progenitor haloes older than $t_{w,\text{peak}} \simeq 2.98$ Gyr (corresponding to formation at $z_1 \gtrsim 13$) is unaffected by environmental effects/cosmic variance, and reflects the average star formation efficiency in the early Universe.
- In such high- z haloes, star formation is episodic on timescales smaller than the age distribution bin size of ~ 50 Myr, such that the luminosity-weighted posterior age distribution of galaxies in XLSSC 122 is a good approximation to the underlying stellar age distribution, assuming a universal mass-to-light ratio.

The observational input comes from the last four bins in the stellar age distribution of XLSSC 122 assuming no dust absorption ($A_V = 0$, see fig. 4 of Willis et al. 2020), corresponding to the four redshift bins: $z_1 \sim 12.6 - 13.6$, $13.6 - 14.8$, $14.8 - 16.3$ and $16.3 - 18.4$ (with *Planck* cosmological parameters, see Sec. 3.1), contributing $\simeq 0.275$, 0.124 , 0.025 and 0.004 of the total stellar mass/luminosity, respectively. Here we focus on the $A_V = 0$ model, as it predicts the oldest stellar ages (up to $z \sim 18$), most relevant for the first galaxies and stars. We build a simple stellar population model for XLSSC 122 with minimum parameters, as described below. With this model, information on high- z

¹ Hydrodynamical simulations of gas in a forming cluster indicate that virial equilibrium is achieved within a minimum of 2 to 3 sound-crossing timescales (Roettiger et al. 1998). We adopt $\Delta t_{\text{obs}} = 3t_{\text{cr}}$ as a conservative estimate of the delay time between cluster formation and observation. In general, lower Δt_{obs} leads to higher HSFE, but the variation is minor (within 30%) for $\Delta t_{\text{obs}} \lesssim 3t_{\text{cr}}$.

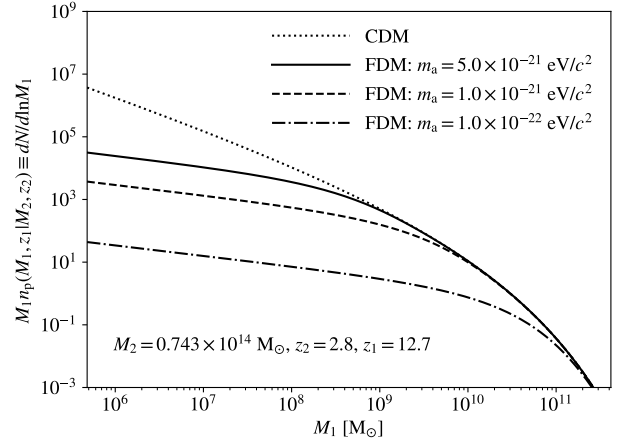


Figure 1. Progenitor mass functions of XLSSC 122 at $z_1 = 12.7$, for the standard Λ CDM (dotted), and FDM models (see Sec. 3.3) with $m_a c^2 = 5 \times 10^{-21}$ eV (solid), 10^{-21} eV (dashed) and 10^{-22} eV (dash-dotted). Here we assume that XLSSC 122 (observed at $z_{\text{obs}} \simeq 1.98$) has a virial mass of $M_2 \sim 10^{14} M_\odot$, and formed 3 sound crossing timescales ago ($t_{\text{cr}} \simeq 3.3 \times 10^8$ yr) at $z_2 \simeq 2.8$, based on X-ray observations (Mantz et al. 2018).

star formation and DM physics can be extracted by matching the observed stellar mass (in galaxies) within a given age range to the model predictions.

Under the episodic star formation assumption, the mass of stars formed in haloes within the mass range $M_1 \sim M_1 + \delta M_1$ and redshift bin i [$z_{1,i} - \Delta z_{1,i}/2; z_{1,i} + \Delta z_{1,i}/2$] is

$$\delta M_{*,i} = \eta(z_{1,i}, M_1) \Delta n_p(z_{1,i}, M_1) M_1 \delta M_1, \quad (1)$$

where $\eta \equiv \langle \Delta M_* \rangle / \Delta M_{\text{halo}} = \eta(z, M_{\text{halo}})$ is the *instantaneous* halo star formation efficiency (HSFE, the average mass of newly-formed stars per increase in halo mass), and $\Delta n_p(z_{1,i}, M_1)$ is the number of progenitor haloes of XLSSC 122 per unit halo mass in the mass range $[M_1; M_1 + \delta M_1]$, formed in redshift bin i . For simplicity, we estimate $\Delta n_p(z_{1,i}, M_1)$ with

$$\Delta n_p(z_{1,i}, M_1) = n_p(z_{1,i} - \Delta z_{1,i}/2, M_1 | z_2, M_2) - n_p(z_{1,i} + \Delta z_{1,i}/2, M_1 | z_2, M_2), \quad (2)$$

where $n_p(z_1, M_1 | z_2, M_2) \equiv dN/dM_1$ is the cluster progenitor mass function² at z_1 , which only depends on cosmology, reflected in the linear power spectrum $P(k)$. Here, we calculate the progenitor mass functions with the standard EPS formalism, without imposing any corrections based on cosmological simulations, which allows us to take into account different cosmologies self-consistently. Fig. 1 shows four examples of n_p for the standard lambda cold dark matter (Λ CDM) cosmology and three fuzzy dark matter (FDM) models (see Sec. 3.3 for details).

We parameterize $\eta(M_1)$ as follows: (i) $\eta = \eta_0$ is constant for $M_1 < M_{\text{low}} = 10^{10} M_\odot$, and (ii) η exhibits (broken) power-law behavior between M_{low} , the peak mass $M_{\text{peak}} = 3 \times 10^{12} M_\odot$, and the high-mass reference point $M_{\text{high}} = 10^{14} M_\odot$ (see Fig. 2 for examples). We set $\eta(M_{\text{peak}}) = 0.02$

² $n_p(z_1, M_1 | z_2, M_2) \delta M_1 \equiv$ number of haloes in the mass range $[M_1; M_1 + \delta M_1]$ at z_1 that end up in a halo of a mass M_2 at z_2 .

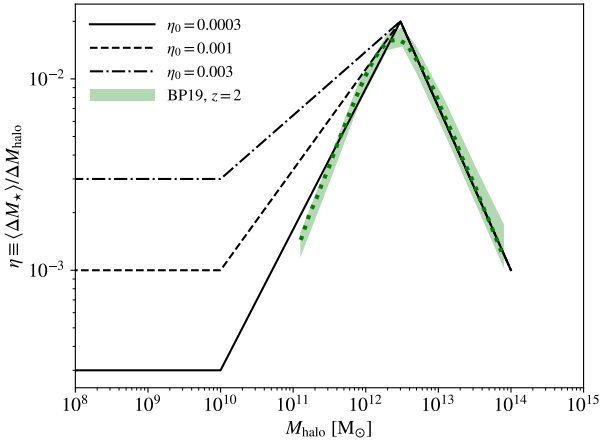


Figure 2. Halo star formation efficiency ($\eta \equiv \langle \Delta M_\star \rangle / \Delta M_{\text{halo}}$) models for $\eta_0 = 3 \times 10^{-4}$ (solid), 0.001 (dashed) and 0.003 (dash-dotted). Here we assume a constant $\eta = \eta_0$ for $M_{\text{halo}} < M_{\text{low}} = 10^{10} M_\odot$, and power laws between M_{low} , the peak mass $M_{\text{peak}} = 3 \times 10^{12} M_\odot$ and the high-mass reference $M_{\text{high}} = 10^{14} M_\odot$. For simplicity, we set $\eta(M_{\text{peak}}) = 0.02$ and $\eta(M_{\text{high}}) = 0.001$, independent of redshift, based on abundance matching results at $z = 2$ in Behroozi et al. 2019 (BP19), shown with the green thick-dotted curve and shaded region for the 68% confidence interval (see their figs. 9 and 10).

and $\eta(M_{\text{high}}) = 0.001$, independent of redshift, based on the abundance matching results at $z = 2$ (Behroozi et al. 2019). Here we assume that η is constant at the low-mass end for simplicity, in agreement with the semi-analytical analysis of Mirocha & Furlanetto (2019) to explain the EDGES 21-cm absorption signal (Bowman et al. 2018). Note that at $z_1 \gtrsim 13$, haloes with $M_1 \lesssim 10^{10} M_\odot$ contribute $\gtrsim 99.9$ (90)% of the total mass of progenitor haloes, such that the behavior of η at $M_1 \gtrsim 10^{10} M_\odot$ is unimportant for star formation at such high redshifts, i.e. $\eta \approx \eta_0$ for $z_1 \gtrsim 13$. Nevertheless, η at the high-mass end is important for determining the total stellar mass $M_{\star, \text{tot}}$ in XLSSC 122 at $z_{\text{obs}} \approx 2$. In our case, $M_{\star, \text{tot}} = M_2 \eta(z=2, M_2) \simeq 10^{11} M_\odot$, according to Behroozi et al. (2019).

Finally, given equations (1) and (2), observation and theory is bridged with

$$f_i M_{\star, \text{tot}} = \int_{M_{\text{th}}}^{M_2} \Delta n_p(z_{1,i}, M_1) M_1 \eta(z_{1,i}, M_1) dM_1. \quad (3)$$

On the left-hand side (observation), f_i is the fraction of stars formed at redshift bin i , while on the right side (theory), there are two unknown/degenerate star formation parameters: $\eta_0(z_{1,i})$ and M_{th} , which is the minimum halo mass for star formation. With equation (3), constraints on M_{th} and $\eta_0(z_{1,i})$ can be derived for any given cosmology embodied by the progenitor mass function $n_p(z_1, M_1 | z_2, M_2)$.

We have thus connected the observed age distribution of galaxies/stars to two key theoretical ingredients: cosmology (n_p) and star formation model (η_0 and M_{th}), which are degenerate to some extent. In a full Bayesian model, the joint posterior distributions of model parameters could be derived once the statistical properties of observational data and priors are available. We defer such complex treatment to future work. Instead, in the following section, we explore

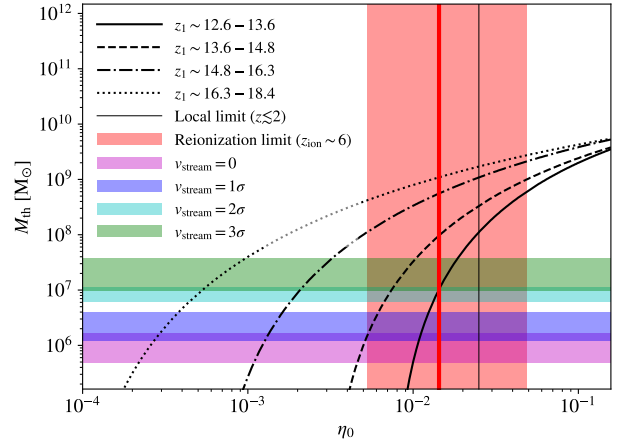


Figure 3. Star formation threshold masses as functions of η_0 for redshift bins $z_1 \sim 12.6 - 13.6$ (solid), $13.6 - 14.8$ (dashed), $14.8 - 16.3$ (dash-dotted) and $16.3 - 18.4$ (dotted). Threshold masses for Pop III star formation from the simulations of Schauer et al. (2019a) are shown with purple, blue, cyan and green shaded regions for 0, 1σ , 2σ and 3σ streaming velocities, respectively. The upper limits on η_0 from reionization (see Sec. 3.2) at $z_{\text{ion}} = 6$ with $\hat{f}_{\text{esc}} = 0.3$ (So et al. 2014) and abundance matching based on local ($z \lesssim 2$) observations (Behroozi et al. 2019) are shown with the thick and thin vertical lines. For the former, the range for $\hat{f}_{\text{esc}} \sim 0.1 - 0.7$ is shown with the red shaded region.

the bounds on individual parameters separately, by fixing a subset of them to existing constraints.

3 CONSTRAINTS ON STAR FORMATION AND DARK MATTER PHYSICS

3.1 Cold dark matter

To begin with, we apply equation (3) to the standard Λ CDM cosmology with *Planck* parameters: $\Omega_m = 0.3089$, $\Omega_b = 0.0486$, $H_0 = 67.74 \text{ km s}^{-1} \text{ Mpc}^{-1}$, $\sigma_8 = 0.8159$, $n_s = 0.9667$, and $N_{\text{eff}} = 3.046$ (Planck Collaboration et al. 2016). The corresponding linear power spectrum $P_{\text{CDM}}(k)$ is obtained from the PYTHON package COLOSSUS³ (Diemer 2018). The resulting constraints on M_{th} and η_0 are shown in Fig. 3, represented by the curves for different redshift bins in $M_{\text{th}} - \eta_0$ space. Generally, the observed stellar mass of a certain age (corresponding to a given redshift bin) is more sensitive to η_0 than M_{th} (for $v_{\text{stream}} \lesssim 3\sigma$), such that 1 dex variation in M_{th} corresponds to less than 0.5 dex variations in η_0 , especially for $z_1 \lesssim 15$.

The degeneracy of η_0 and M_{th} can be broken by further information on either one of them. For illustration, we consider the constraints on M_{th} from the cosmological simulations in Schauer et al. (2019a) with different levels of baryon-DM streaming motion (i.e. $v_{\text{stream}} = 0, 1, 2, 3\sigma$), and the upper limits on η_0 from abundance matching at $z \lesssim 2$ (Behroozi et al. 2019) and reionization (see the next subsection). If we fix M_{th} to the mass above which more than 50% of haloes can form stars, using the results in Schauer

³ <https://bdiemer.bitbucket.io/colossus/>

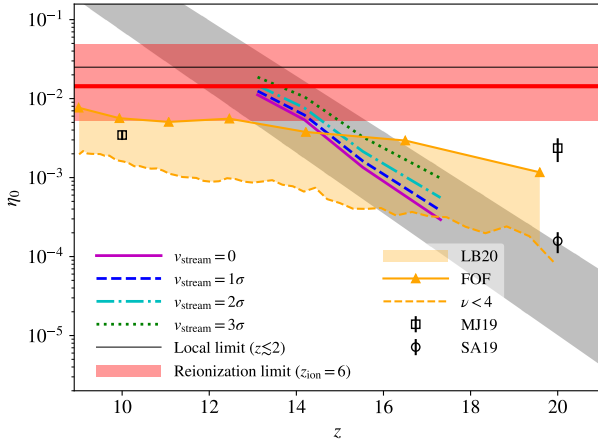


Figure 4. High- z star formation efficiency vs. z , inferred from the stellar age distribution of XLSSC 122 under the $A_V = 0.0$ model (Willis et al. 2020), for 0 (solid), 1σ (dashed), 2σ (dash-dotted) and 3σ (dotted) streaming velocities. The 1σ results are fitted to $\eta_0 \simeq 2.7 \times 10^{-3-0.37(z-15)}$, shown with the gray shaded region (with standard uncertainties). Upper limits on η_0 from reionization (see Sec. 3.2) at $z_{\text{ion}} = 6$ with $\hat{f}_{\text{esc}} = 0.3$ (So et al. 2014) and abundance matching based on local ($z \lesssim 2$) observations (Behroozi et al. 2019) are shown with the thick and thin horizontal lines. For the former, the range for $\hat{f}_{\text{esc}} \sim 0.1 - 0.7$ is shown with the red shaded region. For comparison, we show the estimated η_0 from the EDGES 21-cm absorption signal (Bowman et al. 2018) in the semi-analytical models of Schauer et al. 2019b (SA19; empty circle) and Mirocha & Furlanetto 2019 (MJ19; empty squares), with and without special consideration for Pop III stars, respectively. Cosmological simulation results (Liu & Bromm 2020; LB20) are shown with the orange shaded region, with upper and lower limits denoted by filled triangles (for *star forming* FOF haloes) and the dashed curve (for $\nu < 4$ peaks), respectively.

et al. (2019a), we can derive the redshift evolution of η_0 at different levels of streaming motion, as shown Fig. 4. We find rapid evolution of η_0 with redshift, which is insensitive to streaming motion (within a factor of 4). For instance, we have $\eta_0 \simeq 0.012$, 6.2×10^{-3} , 1.6×10^{-3} and 4×10^{-4} at $z_1 \simeq 13.1$, 14.2 , 15.5 and 17.3 , in the most representative case of 1σ streaming motion. These results can be fitted to an exponential form $\eta_0 \simeq 2.7 \times 10^{-3-0.37(z-15)}$.

We then compare our results with the estimations of η_0 based on the EDGES 21-cm absorption signal (Bowman et al. 2018) in the semi-analytical models from Schauer et al. 2019b (SA19) and Mirocha & Furlanetto 2019 (MJ19), as well as the results from the cosmological simulation in Liu & Bromm 2020 (LB20; their fiducial run `FDbox_Lseed`). For LB20, we consider two definitions of HSFE in simulations: (i) ratio of total increased stellar and halo masses for *star forming* haloes, identified by the ROCKSTAR⁴ halo finder (Behroozi et al. 2012) based on the friends-of-friends (FOF) method, i.e. $\eta_0 = \Delta \left(\sum_j M_{*,j} \right) / \Delta \left(\sum_j M_{\text{halo},j} \right)$, $M_{*,j} > 0$; (ii) ratio of the increased *simulated* stellar mass and increased mass in collapsed objects at $\nu < 4$ peaks predicted by the EPS formalism⁵.

⁴ <https://bitbucket.org/gfcstanford/rockstar/src/master/>

⁵ In detail, $\eta_0 = \Delta M_{*,\text{sim}} / \Delta M_{\text{col}}(\nu < 4)$ with $M_{\text{col}}(\nu < 4) =$

The extrapolated value of η_0 at $z \sim 20$ from our results agrees well with the estimations in SA19⁶ and LB20 for $\nu < 4$ peaks, showing that HSFE is typically low (\sim a few 10^{-4}) for Pop III stars in minihaloes. This is required to not imprint the 21-cm absorption signal at a redshift ($z \gtrsim 20$) higher than observed. Note that similar values ($\sim 10^{-4} - 10^{-3}$) are also found in the recent cosmological simulation from Skinner & Wise (2020). However, in MJ19 and the *star forming* FOF haloes of LB20, the HSFE is almost constant at a higher level (\sim a few 10^{-3}) at $z \sim 10-20$. The detailed analysis of semi-numerical simulations, taking into account the escape fraction of UV photons, also infers that $\eta_0 \sim$ a few 10^{-3} from the observed 21-cm absorption signal (Fialkov & Barkana 2019; Qin et al. 2020). In our case, $\eta_0 \sim$ a few 10^{-3} at $z \sim 14-16$, but it rises to $\sim 10^{-2}$ at $z \sim 13$. The rapid evolution of η_0 may be caused by the fact that XLSSC is likely formed in an overdense region (i.e. at a $\nu \gtrsim 4$ peak).

Note that for LB20, the HSFE based on *star-forming* FOF haloes is higher by a factor of $\sim 3-9$ than that derived from the EPS formalism for $\nu < 4$ peaks (see the orange shaded region in Fig. 4, representing the range in values for the two HSFE methods)⁷. The discrepancies between SA19 and Fialkov & Barkana (2019); Qin et al. (2020) may be caused by different estimations of host halo abundances and treatments for the escape fraction of Lyman- α photons. As significant uncertainties also exist in the input stellar age distribution of XLSSC 122 (Willis et al. 2020), we do not expect the discrepancies found here to have statistical significance. Nevertheless, they indicate that caution is necessary when comparing the results from observations, semi-analytical models and simulations.

3.2 Upper limit from reionization

Another bound on the HSFE can be set by reionization, thus providing a consistency check for our analysis, and also constraining the underlying structure formation history (see the next subsection). We derive an upper limit on η_0 from reionization as follows. First, we define the completion of reionization as the moment when the number of ionizing photons per hydrogen atom reaches two (So et al. 2014),

$V_C \int_{M_{\text{th}}}^{M_{\text{crit}}} M n_h(M) dM$ (as a function of redshift), where V_C is the simulation volume, $n_h(M)$ the EPS halo number density per unit mass, M_{crit} the critical mass for $\nu = 4$ peaks ($\sigma(M_{\text{crit}}) = \delta_c/4$), and $M_{\text{th}} = 1.63 \times 10^6 M_\odot$ according to SA19. Note that the HSFE calculated in this way is lower than that defined for all simulated FOF haloes (i.e. $\eta_0 = \Delta M_{*,\text{sim}} / \Delta \left(\sum_j M_{\text{halo},j} \right)$, $M_{\text{halo},j} > M_{\text{th}}$) by a factor of 2, reflecting the well-known discrepancies between the EPS halo mass functions and those measured in simulations.

⁶ Schauer et al. (2019a) also use the EPS formalism in their analysis, so that their definition of ‘halo’ is consistent with the one adopted in this work.

⁷ This implies that for low-mass haloes at high- z , where the delay time between halo and star formation is non-negligible, most haloes *do not* host stars at a given snapshot. That is to say, the HSFE measured in *star forming* haloes is not representative for the entire halo population, and must be diluted if the average should be taken over *all* haloes.

such that

$$\frac{2X_H \bar{\rho}_b}{m_H} = \dot{N}_{\text{ion}} t_* \hat{f}_{\text{esc}} \times \int_{M_{\text{atm}}}^{\infty} M \eta [n_h(t_{\text{ion}}) - n_h(t_{\text{ion}} - t_*)] dM, \quad (4)$$

where $X_H = 0.76$, $\bar{\rho}_b = 3\Omega_b H_0^2 / (8\pi G)$ is the average baryon density, $\eta \equiv \eta(\eta_{0,z_{\text{ion}}}, M)$ the HSFE parameterized by $\eta_{0,z_{\text{ion}}}$ at z_{ion} , $M_{\text{atm}} = 2.5 \times 10^7 M_{\odot} [(1+z_{\text{ion}})/10]^{-3/2}$ the atomic cooling threshold, and $n_h(t) \equiv n_h(t, M)$ the halo mass function at time t . Further, t_{ion} is the age of the Universe at the end of reionization corresponding to z_{ion} , $t_* \sim 10$ Myr and $\dot{N}_{\text{ion}} = 10^{47} \text{ s}^{-1} M_{\odot}^{-1}$ are the lifetime of O/B stars and luminosity of ionizing photons per unit stellar mass for Population II stars⁸ (which dominate at $z \lesssim 18$, see e.g. Liu & Bromm 2020), and \hat{f}_{esc} is the effective escape fraction. Then we assume that $\eta_{0,z_{\text{ion}}} \geq \eta_0(z_1)$ for $z_1 \gtrsim 13$, such that the upper limit on $\eta_{0,z_{\text{ion}}}$ to not complete reionization before z_{ion} is also the upper limit on $\eta_0(z_1)$, which can be derived by equation (4) given \hat{f}_{esc} and z_{ion} . Here we adopt $z_{\text{ion}} = 6$, and consider the range $\hat{f}_{\text{esc}} \sim 0.1 - 0.7$ with $\hat{f}_{\text{esc}} = 0.3$ the fiducial value, based on the simulations of So et al. 2014 (see also Paardekooper et al. 2015).

As shown in Fig. 3 and 4, the inferred η_0 at $z_1 \gtrsim 13$ is lower than the upper limits set by abundance matching and reionization for $v_{\text{stream}} \leq 2\sigma$, which accounts for $\approx 99\%$ of the cosmic volume, further demonstrating that our results are consistent with existing constraints. Overall, we confirm the emerging picture that star formation began early in cosmic history, but was initially quite inefficient, with a ramp up towards a late epoch of reionization.

3.3 Fuzzy dark matter

Given M_{th} and the upper limit on η_0 either from abundance matching or reionization, our model can also place constraints on the underlying structure formation history (captured by n_p and n_h), governed by DM physics. As an example, we consider the fuzzy dark matter (FDM) scenario, parameterized by the mass of ultra-light particles, m_a , whose linear power spectrum is given by (Hu et al. 2000)

$$\begin{aligned} P_{\text{FDM}}(k) &= T_{\text{FDM}}^2(k) P_{\text{CDM}}(k), \\ T_{\text{FDM}}(k) &= \cos[x_J^3(k)] / [1 + x_J^8(k)], \\ x_J(k) &= 1.61(m_a c^2 / 10^{-22} \text{ eV})^{1/18} (k/k_{J,\text{eq}}), \\ k_{J,\text{eq}} &= 9(m_a c^2 / 10^{-22} \text{ eV})^{1/2} \text{ Mpc}^{-1}. \end{aligned} \quad (5)$$

As shown in Hirano et al. (2018), star formation can be significantly delayed to occur in more massive structures in FDM models, compared with standard Λ CDM. Therefore, the mass of old stars in XLSSC 122 can constrain the parameter m_a , once η_0 and M_{th} are known. For simplicity, we

⁸ Here we neglect the contribution of Pop III stars to completing reionization at $z_{\text{ion}} \sim 6$, as Pop III star formation will be significantly suppressed by external Lyman-Werner and ionizing photons, as well as metal enrichment. Previous studies have found that the Pop III contribution to the ionizing photon budget is $\lesssim 10\%$ (e.g. Greif & Bromm 2006; Wise et al. 2011; Paardekooper et al. 2015).

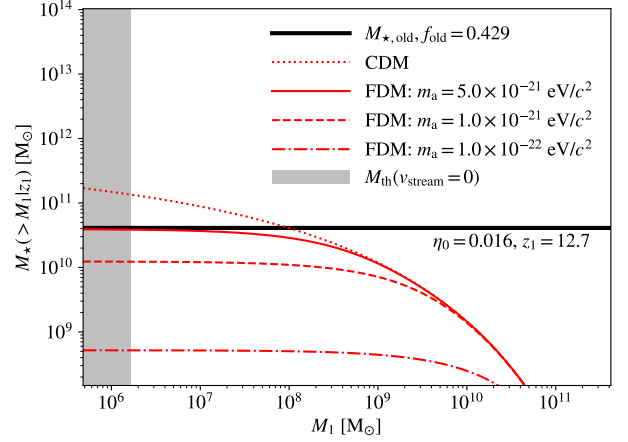


Figure 5. Cumulative stellar mass from the progenitors of XLSSC 122 at $z_1 = 12.7$, for the standard Λ CDM (dotted), and FDM models with $m_a c^2 = 5 \times 10^{-21}$ eV (solid), 10^{-21} eV (dashed) and 10^{-22} eV (dash-dotted). Here $\eta_0 = 0.016$ is set to the fiducial upper limit (with $\hat{f}_{\text{esc}} = 0.3$) placed by reionization at $z_{\text{ion}} = 6$ (So et al. 2014) for the critical FDM model with $m_a c^2 = 5 \times 10^{-20}$ eV. The total mass of old galaxies (older than 2.98 Gyr, i.e. formed at $z > z_1$) in XLSSC 122 is shown with the thick horizontal line, which makes up $f_{\text{old}} \simeq 0.43$ of the total stellar mass. The shaded region shows the range of halo mass in which up to 50% of haloes have star formation from Schauer et al. (2019a) without streaming motion. The FDM models that never cross the $M_{*,\text{old}}$ line are ruled out.

now consider all the redshift bins together⁹ for stars/galaxies older than 2.98 Gyr, which accounts for $f_{\text{old}} \simeq 0.43$ of the total stellar mass, and rewrite equation (3) at $z_1 \simeq 12.7$ as

$$M_{*,\text{old}} = \int_{M_{\text{th}}}^{M_2} n_p(M_1) M_1 \eta(\eta_0, M_1) dM_1, \quad (6)$$

where $n_p(M_1) \equiv n_p(z_1, M_1|z_2, M_2)$ (see Fig. 1), and $M_{*,\text{old}} = f_{\text{old}} M_{*,\text{tot}}$. There exists a lower limit $m_{a,\text{min}}$ below which the above equation (6) cannot be satisfied with reasonable M_{th} and η_0 , when structure formation is delayed to lower redshifts $z \lesssim z_1 \simeq 12.7$.

To derive a conservative estimate for this lower limit, we set M_{th} to the lowest threshold value of $\simeq 5 \times 10^5 M_{\odot}$, which is the minimum mass of star formation in Schauer et al. (2019a) with no streaming motion¹⁰, and η_0 to the (fiducial) upper limit from reionization $\eta_{0,\text{max}}$ (with $\hat{f}_{\text{esc}} = 0.3$), given by equation (4). Note that here both the halo mass function n_h and the progenitor mass function n_p depend on m_a , so that equations (3) and (5) must be solved together for $\eta_{0,\text{max}}$

⁹ Actually η_0 here stands for the *cumulative* HSFE for $z \gtrsim z_1 \simeq 12.7$. We assume that the HSFE generally increases with decreasing redshift before reionization, so that the cumulative HSFE should be smaller than the instantaneous one at a given redshift. Therefore, our constraints on m_a should be regarded conservative when any upper limit on the *instantaneous* HSFE is adopted.

¹⁰ It turns out that $m_{a,\text{min}}$ is not sensitive to M_{th} for $M_{\text{th}} \lesssim 10^7 M_{\odot}$ (i.e. $v_{\text{stream}} \lesssim 2\sigma$), since for typical FDM models with $m_a \lesssim 10^{-20}$ eV/ c^2 , the contribution from minihaloes ($M_{\text{halo}} \lesssim 10^7 M_{\odot}$) to the total stellar mass formed at $z \gtrsim z_1 \simeq 12.7$ is negligible (see Fig. 5).

and $m_{a,\min}$. Carrying out these steps, we find $\eta_{0,\max} \simeq 0.016$ and $m_{a,\min} \simeq 5 \times 10^{-21} \text{ eV}/c^2$.

This approach is further illustrated in Fig. 5 in terms of the cumulative stellar mass $M_*(> M_1)$, where FDM models with $M_*(> M_{\text{th}}) < M_{*,\text{old}}$ are ruled out. If we adopt $\eta_0 = 0.025$, which is the local ($z \lesssim 2$) upper limit from abundance matching (Behroozi et al. 2019), equation (6) can be solved independently to give a weaker constraint on FDM of $m_{a,\min} \simeq 2.5 \times 10^{-21} \text{ eV}/c^2$. Using the reionization upper limit with $\hat{f}_{\text{esc}} = 0.1$ leads to an even weaker constraint of $m_{a,\min} \simeq 6 \times 10^{-22} \text{ eV}/c^2$ for $\eta_{0,\max} \simeq 0.091$, which is unphysical, as it would imply that $\sim 60\%$ of baryons end up in stars. Interestingly, our constraints on FDM inferred from the cluster XLSSC 122 are consistent with those based on the EDGES 21-cm absorption signal (Bowman et al. 2018), e.g. $m_{a,\min} \simeq 5 \times 10^{-21} \text{ eV}/c^2$ in Lidz & Hui (2018) and $m_{a,\min} \simeq 8 \times 10^{-21} \text{ eV}/c^2$ in Schneider (2018).

4 SUMMARY AND CONCLUSIONS

We demonstrate a new approach of indirectly constraining early star and structure formation via mature galaxy clusters at cosmic noon ($z \sim 2$), using the cluster XLSSC 122 as an example ($z_{\text{obs}} = 1.98$). Based on the age distribution of galaxies/stars in XLSSC 122 (neglecting dust extinction) measured by HST photometry (Willis et al. 2020), and its halo properties from X-ray observations (Mantz et al. 2018), we infer a rapid evolution of the halo star formation efficiency (HSFE, $\eta \equiv \langle \Delta M_* \rangle / \Delta M_{\text{halo}}$) at $z \sim 13 - 18$. Specifically, we derive a fit $\eta \simeq 2.7 \times 10^{-3-0.37(z-15)}$ for low-mass haloes ($M_{\text{halo}} \lesssim 10^{10} M_{\odot}$) that host the first stars and galaxies. Our results generally agree with semi-analytical models based on 21-cm absorption and cosmological simulations, giving $\eta_0 \sim 10^{-4}$ to a few 10^{-3} at $z \sim 13 - 20$ (Mirocha & Furlanetto 2019; Schauer et al. 2019b; Fialkov & Barkana 2019; Qin et al. 2020; Skinner & Wise 2020; Liu & Bromm 2020). However, such rapid evolution is unique to our model, likely caused by the fact that XLSSC is formed in an overdense region, corresponding to a $\nu \gtrsim 4$ peak.

We also place new constraints on the mass of ultra-light bosons in fuzzy dark matter models of $m_a \lesssim 5 \times 10^{-21} \text{ eV}/c^2$, from the abundance of star forming galaxies at $z \gtrsim 13$ in the merger tree of XLSSC 122. This is comparable to existing constraints $m_a \lesssim 5 - 8 \times 10^{-21} \text{ eV}/c^2$ (Lidz & Hui 2018; Schneider 2018).

However, significant uncertainties exist in the inferred stellar age distribution of XLSSC 122, as the posterior age distributions of individual galaxies are broad ($\sim \text{Gyr}$). This is typical for photometry-inferred ages (see fig. 7-8 in Andreon et al. 2014 and extended data fig. 2-3 of Willis et al. 2020). The age distribution is also sensitive to the underlying stellar population parameters assumed for SED fitting (e.g. IMF, metallicity and star formation history), especially the assumption on dust absorption (Willis et al. 2020). We here focus on the zero-dust absorption ($A_V = 0$) model that predicts major star formation to occur around $z \sim 12$ and extend to $z \sim 18$, while in models with dust absorption (e.g. $A_V = 0.3$ and 0.5) the stellar population is shifted to lower redshifts ($z \sim 6 - 13$), becoming less relevant to the first stars and galaxies.

Besides, it remains unknown whether XLSSC 122 is an

extreme case or a typical galaxy cluster at $z \sim 2$. Therefore, our results should be regarded as tentative and for illustration purpose. Nevertheless, more comprehensive results will be obtained if our approach is extended to a large sample of clusters or field post-starburst galaxies at cosmic noon, with a full statistical framework in which observational uncertainties are properly propagated to the inferred star/structure formation parameters. There is thus a strong case for systematic observational campaigns to identify galaxy clusters at cosmic noon and to characterize their member galaxies.

On the theoretical side, we use the standard EPS formalism for simplicity and flexibility in the current work, which defines haloes differently from cosmological simulations. This introduces an additional layer of complexity for bridging theory and observation, given that simulations are needed to implement the detailed physics of star and galaxy formation, such as primordial chemistry, cooling and stellar feedback. In future work, merger trees constructed from simulations should be used to calculate the progenitor mass functions of clusters. That approach does not only remove the ambiguity in halo definition but also enables one to account for cosmic variance. We may also use more physically motivated models of the HSFE that allow variation with halo mass at $M_{\text{halo}} \lesssim 10^{10} M_{\odot}$, reflecting the different modes of early star formation in atomic cooling haloes ($M_{\text{halo}} \gtrsim 10^7 M_{\odot}$) and molecular cooling minihaloes ($M_{\text{halo}} \sim 10^6 M_{\odot}$).

Overall, we begin to probe the earliest epoch of star and galaxy formation with the tantalizing hints provided by pioneering observations, such as the ones discussed here. Soon, we will be able to complement this with direct observations of active star formation at the highest redshifts, together contributing to the emerging model of the first stars and galaxies.

ACKNOWLEDGMENTS

Support for this work was provided by NASA through the NASA Hubble Fellowship grant HST-HF2-51418.001-A awarded by the Space Telescope Science Institute, which is operated by the Association of Universities for Research in Astronomy, Inc., for NASA, under contract NAS5-26555.

REFERENCES

- Andreon S., Newman A., Trinchieri G., Raichoor A., Ellis R., Treu T., 2014, *A&A*, 565, A120
- Appleton P., et al., 2009, in *astro2010: The Astronomy and Astrophysics Decadal Survey*. p. 2 ([arXiv:0903.1839](https://arxiv.org/abs/0903.1839))
- Basu-Zych A., et al., 2019, in *Bulletin of the American Astronomical Society*.
- Behroozi P. S., Wechsler R. H., Wu H.-Y., 2012, *ApJ*, 762, 109
- Behroozi P., Wechsler R. H., Hearin A. P., Conroy C., 2019, *MNRAS*, 488, 3143
- Bowman J. D., Rogers A. E. E., Monsalve R. A., Mozdzen T. J., Mahesh N., 2018, *Nature*, 555, 67
- Bromm V., 2013, *Rep. Prog. Phys.*, 76, 112901
- Bromm V., Yoshida N., 2011, *ARA&A*, 49, 373
- Diemer B., 2018, *ApJS*, 239, 35
- Fialkov A., Barkana R., 2019, *MNRAS*, 486, 1763
- Frebel A., Norris J. E., 2015, *ARA&A*, 53, 631
- Gobat R., et al., 2013, *ApJ*, 776, 9

- Greif T. H., Bromm V., 2006, *MNRAS*, 373, 128
- Hartwig T., Bromm V., Klessen R. S., Glover S. C. O., 2015, *MNRAS*, 447, 3892
- Hirano S., Sullivan J. M., Bromm V., 2018, *MNRAS*, 473, L6
- Hu W., Barkana R., Gruzinov A., 2000, *Phys. Rev. Lett.*, 85, 1158
- Ishigaki M. N., Tominaga N., Kobayashi C., Nomoto K., 2018, *ApJ*, 857, 46
- Jeon M., Bromm V., 2019, *MNRAS*, 485, 5939
- Ji A. P., Frebel A., Bromm V., 2015, *MNRAS*, 454, 659
- Lidz A., Hui L., 2018, *Phys. Rev. D*, 98, 023011
- Liu B., Bromm V., 2020, arXiv e-prints, p. [arXiv:2003.00065](https://arxiv.org/abs/2003.00065)
- Loeb A., Furlanetto S. R., 2013, *The First Galaxies in the Universe*. Princeton Univ. Press, Princeton, NJ
- Magg M., Klessen R. S., Glover S. C., Li H., 2019, *MNRAS*, 487, 486
- Maggiore M., et al., 2020, *J. Cosmology Astropart. Phys.*, 2020, 050
- Mantz A. B., et al., 2018, *A&A*, 620, A2
- Mirocha J., Furlanetto S. R., 2019, *MNRAS*, 483, 1980
- Mo H., Van den Bosch F., White S., 2010, *Galaxy formation and evolution*. Cambridge University Press
- Newman A. B., Ellis R. S., Andreon S., Treu T., Raichoor A., Trinchieri G., 2014, *ApJ*, 788, 51
- Paardekooper J.-P., Khochfar S., Dalla Vecchia C., 2015, *MNRAS*, 451, 2544
- Pawlik A. H., Milosavljević M., Bromm V., 2011, *ApJ*, 731, 54
- Planck Collaboration et al., 2016, *A&A*, 594, A13
- Qin Y., Mesinger A., Park J., Greig B., Muñoz J. B., 2020, arXiv e-prints, p. [arXiv:2003.04442](https://arxiv.org/abs/2003.04442)
- Roettiger K., Stone J. M., Mushotzky R. F., 1998, *ApJ*, 493, 62
- Schauer A. T., Glover S. C., Klessen R. S., Ceverino D., 2019a, *MNRAS*, 484, 3510
- Schauer A. T., Liu B., Bromm V., 2019b, *ApJ*, 877, L5
- Schneider A., 2018, *Phys. Rev. D*, 98, 063021
- Skinner D., Wise J. H., 2020, *MNRAS*, 492, 4386
- So G. C., Norman M. L., Reynolds D. R., Wise J. H., 2014, *ApJ*, 789, 149
- Stanford S., et al., 2012, *ApJ*, 753, 164
- Strazzullo V., et al., 2016, *ApJ*, 833, 6pp
- Willis J., et al., 2020, *Nature*, 577, 39
- Wise J. H., Turk M. J., Norman M. L., Abel T., 2011, *ApJ*, 745, 50
- Zackrisson E., et al., 2017, *ApJ*, 836, 78

This paper has been typeset from a \LaTeX file prepared by the author.